Medical & Biological Engineering & Computing
https://doi.org/10.1007/s11517-022-02716-8

ORIGINAL ARTICLE

Computational analysis of human upper airway aerodynamics

Rutger H.J. Hebbink[1] · Bas J. Wessels[1] · Rob Hagmeijer[1] · Kartik Jain[1]

Received: 14 February 2022 / Accepted: 7 November 2022

Abstract

There is a considerable interest in understanding transient human upper airway aerodynamics, especially in view of assessing the effects of various ventilation therapies. Experimental analyses in a patient-specific manner pose challenges as the upper airway consists of a narrow confined region with complex anatomy. Pressure measurements are feasible, but, for example, PIV experiments require special measures to accommodate for the light refraction by the model. Computational fluid dynamics can bridge the gap between limited experimental data and detailed flow features. This work aims to validate the use of combined lattice Boltzmann method and a large eddy scale model for simulating respiration, and to identify clinical features of the flow and show the clinical potential of the method. Airflow was computationally analyzed during a realistic, transient, breathing profile in an upper airway geometry ranging from nose to trachea, and the resulting pressure calculations were compared against in vitro experiments. Simulations were conducted on meshes containing about 1 billion cells to ensure accuracy and to capture intrinsic flow features. Airway pressures obtained from simulations and in vitro experiments are in good agreement both during inhalation and exhalation. High velocity pharyngeal and laryngeal jets and recirculation in the region of the olfactory cleft are observed.

Keywords Lattice Boltzmann method · Nasal cavity · Respiration · High performance computing

1 Introduction

The human nasal airways provide the body with oxygen-rich air during inhalation and remove carbon dioxide-rich air during exhalation. In addition to this, the nose heats, humidifies, and filters inhaled air, and allows for the sense of smell. All of these functions depend strongly on the flow field in the nasal cavity which therefore has received considerable attention over the last decades. Nasal flow has been visualized by using smoke particles in air-filled models and by using dye in liquid-filled models, but this method is only qualitative and not quantitative [10]. More recently, velocities were measured experimentally using various forms of particle image velocimetry (PIV) [7, 40, 41, 50]. Although detailed information can be obtained from these measurements, the time and effort needed to construct PIV models and to perform the experiments are considerable. As a result, computational fluid dynamics (CFD) has risen as a potential alternative that can give quantitative information about the flow in nasal cavities [7, 10, 32].

Riazuddin et al. [36] simulated several steady inspiratory and expiratory flows through the nasal cavity, assuming the flow to be laminar up to 15 L/min and using a turbulence model at higher flow rates. Recirculation was observed in the olfactory region during inhalation, and in the posterior region of the nasal cavity during exhalation. Fomin et al. [14] simulated inhalation by prescribing constant pressure differences, showing that the inspiratory flow fields differed significantly between three nasal geometries. The variation of the nasal airflow pattern with nasal morphology was confirmed in other computational studies [51, 52]. A study on the steadiness of flow in the nasal cavity revealed that steady and unsteady pressure losses are different, although the difference could be neglected around higher mass fluxes (i.e., near the inspiratory and expiratory peaks) [23]. Lee et al. [30] confirmed and quantified the differences between steady and unsteady computations with a large eddy scale (LES) model.

Many studies focused on the nasal cavity only, but also other parts of the upper airway have been studied.

✉ Kartik Jain
k.jain@utwente.nl

Rutger H.J. Hebbink
r.h.j.hebbink@utwente.nl

[1] Engineering Fluid Dynamics, Faculty of Engineering Technology, University of Twente, P.O. Box 217, 7500 AE, Enschede, The Netherlands

Published online: 20 December 2022

Wang et al. [48] simulated a sinusoidal breathing pattern in a model ranging from nose to triple bifurcation (without sinuses), showing that flow in the trachea and pharynx was different during inhalation (along posterior of airway) than exhalation (along centreline). In [49], three realistic models from nose to trachea are shown to have different flow fields during steady inhalation. The heat transfer within the upper airway has been simulated both during inhalation of hot air [16] and during respiration in air at room temperature [34]. Other studies focused on oral breathing in idealized [6, 8, 9] or realistic [43] models from mouth to trachea, showing that the glottis greatly influences the flow field.

Most of the CFD simulations assumed either laminar flow or turbulent flow described by the Reynolds-averaged Navier-Stokes (RANS) equations supplemented with turbulence models. However, the averaging procedure reduces the accuracy of the simulations. Xu et al. [50] performed RANS simulations and compared the flow in the trachea obtained with three different turbulence models to PIV experiments. The results show that the best model differed both with tracheal cross-section and flow rate during inhalation, but that there was little difference between the turbulence models during exhalation. It is noted that the flow fields were only compared in the trachea, whereas the effects of turbulence during exhalation are especially expected from the larynx upwards [8, 9, 50]. Mihaescu et al. [33] showed that (steady) RANS simulations could not reproduce relevant flow features in the airway, and suggested that LES simulations should be preferred.

Although computational studies have proven to be useful to better understand the flow phenomenon in the nasal cavity [36], only very few studies have used the preferred LES or direct numerical simulation (DNS). The large differences observed in the flow patterns in different geometries justify the simulation of new geometries, especially since the velocity field in an averaged geometry was quite different from individual geometries [5]. In particular, there is a lack of unsteady simulations with a full breathing cycle using LES or DNS, which will therefore be the scope of this study.

All of the above-mentioned studies employed the finite volume method (FVM), but the required generation of the boundary conforming meshes in the nasal cavity with its complex geometry and narrow flow channels is cumbersome and time consuming [10]. Moreover, the detailed capture of flow features requires a fine grid in the simulations, which consequently requires deployment of a method that can scale well on massively parallel supercomputers. The lattice Boltzmann method (LBM), being an explicit numerical scheme, allows for excellent scalability on supercomputers [26]. The staircase approximation at the boundaries, while problematic has been circumvented by recent developments in higher order wall boundary conditions within the LBM [4]. The LBM itself and the solver employed in this study, *Musubi*, have also been validated in previous work [25] against the nozzle benchmark set by the US food and drug administration (FDA). A comparison of LBM to FVM for laminar, incompressible, and steady inhalation and exhalation showed that LBM is indeed a well-suited candidate for efficient flow prediction [15]. Lintermann et al. [32] used LBM to compare the pressure loss, wall shear stress, and heating capability in three different nasal geometries during steady inhalation, again showing large differences between the geometries. Although LBM is able to resolve very small scales, it may be combined with LES to reduce computational effort and still yield high resolution flow fields. This combination was used to simulate constant inhalation and exhalation in the nasal cavity and shown to be in good agreement with FVM solutions [13]. Berger et al. [2, 3] used LBM/LES in a pre-operative surgical prediction tool with constant breathing flow rates in the nasal cavity, demonstrating that fast and accurate solutions are obtained. Combined LBM/LES is considered an excellent computational method to accurately and efficiently compute transient upper airway flows, but it has, to the authors' knowledge, not been used before in this application.

The objective of this work is twofold. The first objective is to validate the use of combined LBM/LES for simulating dynamic respiration in a realistic upper airway geometry against experiments. The second objective is to use the high resolution flow fields to identify important clinical features of the flow and show the clinical potential of the method.

The present study presents numerical simulations of a full breathing cycle in an upper airway geometry down to the trachea using a combination of LBM and LES. The simulations have been validated by comparing computed pressure data with pressure data obtained from laboratory experiments on a 3D-printed version of the airway geometry considered. First, the airway geometry is presented in Section 2, and then LBM/LES (Section 2.1) and the experimental setup (Section 2.2) are described. In Section 3, the numerical and experimental data are presented and compared, and the accuracy is analyzed. Finally, the flow field and its clinical relevance are discussed in Section 4.

2 Methods

This work focuses on the respiratory flow in the human upper airway from nose to trachea. The first part of the upper airway is the nasal cavity, which is a very complex anatomical structure. The visible nose is only about a third of the whole cavity. The nasal cavity as a whole consists of two chambers which are about 50 mm high and 100 mm long, making up for a total surface area of 15,000 mm^2 and a total volume of 15 mL. The nose is enclosed with sinuses,

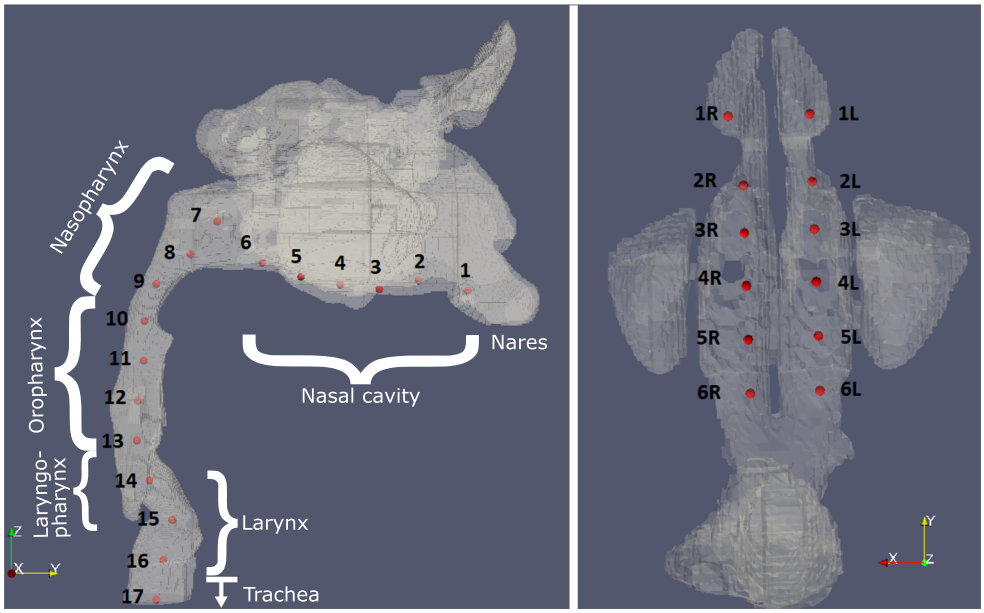

Fig. 1 Side and bottom views of the upper airway. The image represents the fluid domain which was used for computations. The various points indicate the probes where pressure was measured in experiments and simulations for comparison, and the names of the different airway regions are indicated

which under normal circumstances are filled with air that undergoes a full change every few hours. The airflow in the nose is controlled by the shape of the internal passages. The two nasal cavities merge in the nasopharynx. The geometry then diverges towards the oropharynx, where the mouth is connected to the airway. In this work, a geometry is used where the oral connection is closed, and hence the mouth is not present. The geometry converges towards the larynx and diverges again towards the trachea.

A freely available 3D surface model of an adult male with closed mouth, based on a CT scan, was obtained in STL format from [11]. Author permission was granted to modify and use the geometry for research purposes. The used (modified) geometry is shown in Fig. 1.

2.1 Computational method

2.1.1 Governing equations

A fluid flow in the nasal cavity can be described by the Navier-Stokes equations (NSE):

$$\frac{\partial}{\partial t}(\rho u_i) + \sum_{j=1}^{3}\left[\frac{\partial}{\partial x_j}(\rho u_i u_j) - \frac{\partial \sigma_{ij}}{\partial x_j}\right] - \rho g_i = 0, \forall(\mathbf{x}, t) \tag{1}$$

where u is the fluid velocity, ρ the density, g the gravitational acceleration, and σ the stress tensor. An additional condition for a divergence-free velocity field is employed in an incompressible flow:

$$\sum_{j=1}^{3}\frac{\partial u_j}{\partial x_j} = 0. \tag{2}$$

This work employed the LES turbulence model. In LES, only flow structures on a large scale are resolved directly while the smaller structures are considered residual and need to be modelled adequately. The residual scales are separated from the resolved scales by applying a filter to the unknown quantities [31]. Applying the filtering process to the NSE and collecting the additionally obtained quantities into a residual stress tensor τ^r leads to the filtered equations of motion for incompressible, Newtonian fluids for the filtered quantities $\bar{\phi}$.

The LBM is based on the mesoscopic representation of movement of fictitious particles. Each of these particles has discrete velocities and they collide and stream to relax towards a thermodynamic equilibrium. The lattice Boltzmann (LB) equation recovers the NSE under the continuum limits of low Mach and Knudsen numbers. Evolution of the particles over time is described by the LB equation with the multi-relaxation time (MRT) collision matrix:

$$f_i(\mathbf{r}+\mathbf{c}_i\delta t, t+\delta t) = f_i(\mathbf{r}, t)+\Omega_{ij}\left(f_i^e(\mathbf{r}, t) - f_i(\mathbf{r}, t)\right) \tag{3}$$

where f_i represents the density distributions of particles which are moving with discrete velocity $\mathbf{c}_i$ at a position $\mathbf{r}$ at time t. The indices which run from $i = 1 \ldots Q$ denote the links per element, i.e., the discrete directions, depending on the chosen stencil (D3Q19 in this work). The collision matrix Ω_{ij} defines relaxation of various modes of the distribution functions f_i towards an equilibrium f_i^e:

$$f_i^e = w_i\rho\left(1 + \frac{\mathbf{c}_i\cdot\mathbf{u}}{c_s^2} - \frac{\mathbf{u}^2}{2c_s^2} + \frac{1}{2}\frac{(\mathbf{c}_i\cdot\mathbf{u})^2}{c_s^4}\right) \tag{4}$$

where w_i are the weights for each discrete link, c_s is the reference speed of sound in LBM obtained by integration of the discrete Boltzmann equation along characteristics, and

u is the fluid velocity. The time step in LBM is coupled with the grid size by $\delta t \sim \delta x^2$ due to *diffusive* scaling which is employed to recover the incompressible NSE. Details on the computation of macroscopic quantities from LBM can be found elsewhere [42].

In LBM, the LES model is implemented by adding viscosity via locally increasing the relaxation parameter ω, which damps short wave-length oscillations. Detailed implementations of this model are described by Krafczyk et al. [29] and Hasert [19]. The (MRT) collision operator of the LB equation was employed to ensure stability. A detailed validation of the LBM solver *Musubi* for the simulation of physiologic flows has been described by Jain [25].

2.1.2 The simulation framework

The employed simulation tool-chain is contained in the end-to-end parallel framework APES (adaptable poly engineering simulator) [28, 38].[1] Meshes are created using the mesh generator *Seeder* [17] and computations are carried out using the LBM-based solver *Musubi* [20]. *Musubi* writes out binary files containing physics information to the disk. These files are converted to the visualization toolkit (VTK) format by the post-processing tool *Harvester*, which is contained within the APES framework. The open source visualization tool Paraview[2] is then used to visualize the physics of flow. The data for plots is written out by *Musubi* as ASCII files that are plotted using the Matplotlib plotting library within the Python programming language.

The 3D model of the upper airway is shown in Fig. 1. Pressure was probed at various points shown in the image and was then compared in both experiments and simulations. The 3D model in STL format was fed to the mesh generator *Seeder* that created volume meshes and saved them to the disk. A higher order wall boundary condition described by Bouzidi et al. [4] was prescribed at the walls of the nasal cavity to reduce the influence of staircase artifacts in LBM and ensure rotational symmetry of the D3Q19 lattice. Previous works have shown that a combination of higher spatial resolution and this boundary condition negates the influence of staircase approximations [26]. An in vivo measured breathing waveform of a healthy 24-year-old male was obtained from literature [45]. The breathing profile was scaled to take 4 s, and the resulting flow-time curve is shown in Fig. 2. Throughout this work, exhalation is defined as positive and inhalation is denoted with negative flow rates. A velocity profile corresponding to the breathing cycle was used as inlet boundary condition while a zero pressure was maintained at the outlet. Note that during inhalation the nostrils are the inlet and the trachea is the outlet, whereas this is reversed during exhalation. For exhalation, the pressures were shifted afterwards to obtain atmospheric nostril pressure throughout the breathing cycle. The inhalation phase of the breathing cycle takes about 1.78 s from the total breathing cycle. Peak inhalation occurs at 0.98 s with a flow rate of −22.13 L/min. During this peak, the velocity inlet in the left and right nostrils reaches about 1589 mm/s and 1071 mm/s respectively. This corresponds to a Reynolds number of 1411 and 680 in the left and right nostril respectively. The exhalation phase takes 2.216 s. The peak flow occurs at 1.168 s during exhalation resulting in a volume flow rate of 16 L/min. This corresponds to a maximum inlet velocity of 2955 mm/s at the trachea.

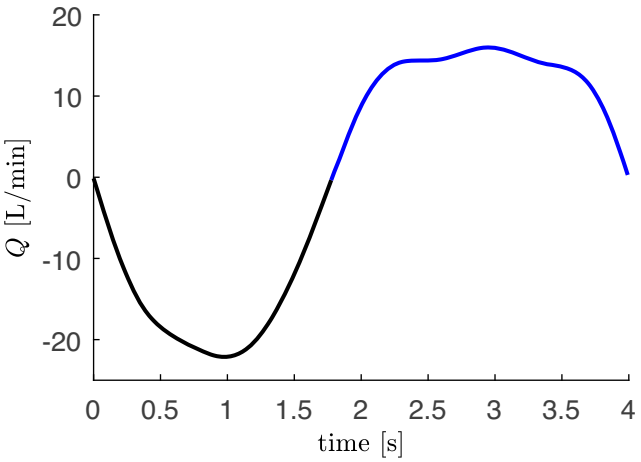

Fig. 2 The breathing profile used as inflow boundary condition in the simulations. The black (negative) part shows the inhalation phase while the blue (positive) part of the cycle shows the exhalation phase

2.1.3 Boundary conditions

During exhalation, the inlet velocity profile at the trachea was prescribed to be fully developed (i.e., parabolic). During inhalation, flow was prescribed to have a uniform velocity profile at the nostrils. The inspiratory flow was divided over both nostrils such that the pressure at both nostrils was equal. The required flow ratio was determined from low Reynolds number simulations. At peak inhalation, 62% of the flow was prescribed to the left nostril. Flow was allowed to develop for one cycle and the characteristics were analyzed during the second breathing cycle. A mesh convergence study was carried out as described in the Appendix, and it was found that spatial and temporal resolutions of approximately 48 μm and 0.62 μs respectively would be required for accurate simulations of flow dynamics during unassisted breathing. This resolution resulted in about 925 million lattice sites. Due to the high Reynolds number in the

[1] https://apes.osdn.io

[2] https://www.paraview.org

flow, a full direct numerical simulation (DNS) would have required about 2.6 billion cells [25]. In a set of simulations performed with a lower Reynolds number, it was observed that only some small regions had large fluctuations, an observation that negated the need for a fully resolved DNS. Hence, a LES turbulence model was employed within the LBM framework using the Smagorinsky model.

2.2 Experimental method

The computations were compared to lab experiments on a 3D-printed version of the geometry, which was described in detail in previous works [21, 22]. A total of 23 pressure locations, with approximately 10 mm spacing, were added to the original (digital) model: 6 in both sides of the nasal cavity and the remaining 11 in the nasopharynx to trachea. The reader is referred to [21] for details about the placement of the pressure taps in the model and the 3D-printing. The post-processed 3D-printed geometry is shown in Fig. 3. Data was recorded using two pressure scanners (NetScanner model 9216, Measurement Specialities, Les Clayes-sous-Bois, France), with a sampling time of 6 ms (167 Hz).

A breathing simulator was connected to the trachea of the 3D-printed model to simulate respiration. The breathing simulator consisted of a pneumatic cylinder rigidly connected to a linear motor, as was described in a previous study [22]. The motion of the motor in time was prescribed, such that the volume displaced by the pneumatic cylinder matched the desired breathing profile. Similar to a previous study, the pressure was recorded while repeating the breathing pattern for 100 s to obtain approximately 25 breathing cycles [21]. A low-pass filter of 2.5 Hz (ten times the breathing frequency) was applied to the data [22]. The experimental pressures were calculated as the average of the individual full breathing cycles in the 100 s measurement [21].

2.3 Flow characterization method

The numerical and experimental flows were compared based on the pressures at the different pressure locations. The pressures were compared based on the maximum (exhalation) or minimum (inhalation) value, representing peak exhalation or inhalation, and on the mean value during exhalation and inhalation. The mean pressure values are closer to zero, but also less sensitive to fast temporal pressure variations than the peak pressures. The average value of the maximum pressures of all breathing cycles was taken as the experimental maximum pressure, and the minimum pressure was calculated similarly. The mean pressures were calculated as the average of all positive (exhalation) or negative (inhalation) pressure samples.

Due to a mistake in its location specification in the simulations of inhalation, point 11 has not been taken into account in the pressure comparison of inhalation.

3 Results

First a comparison of experiments and simulations is given, followed by a demonstration of insights into flow features obtained from the simulations. The location of the pressure points and the named airway regions are indicated in Fig. 1.

3.1 Experiments and simulation comparison

The mean and minimum pressures during inhalation are plotted for both simulations and experiments in Fig. 4a and b respectively. In general, the trend of the mean pressures from simulations and experiments is in good agreement, except for the first points in both nostrils (1L and 1R). In these points, the numerical pressure is close to zero (atmospheric), whereas the experimental pressure is close to

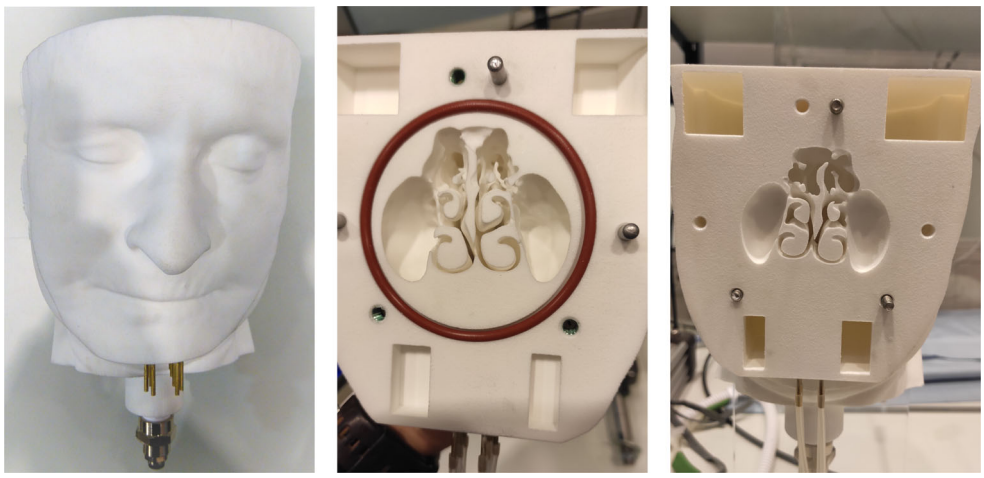

(a) External (b) Posterior view (c) Anterior view

Fig. 3 Pictures of the outside and inside of the 3D-printed geometry

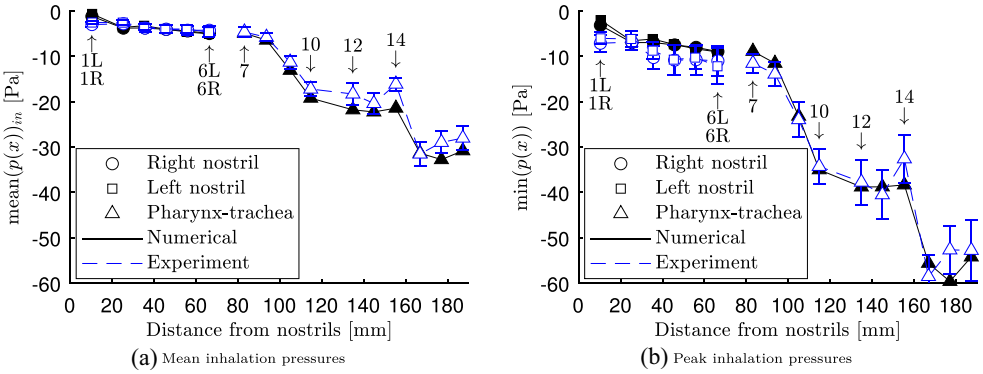

(a) Mean inhalation pressures (b) Peak inhalation pressures

Fig. 4 Inhalation: comparison of pressure obtained from simulations (filled symbols, black) and experiments (open symbols, blue) at the locations depicted in Fig. 1. Error bars for experimental data indicate ±standard deviation of the corresponding values from the individual full breathing cycles

the second point in both nostrils. The absolute differences are only 1.8 and 1.9 Pa (1R and 1L, respectively), but this results in relative differences of 61 and 75%. The maximum deviation is approximately 5.3 Pa (33%) at point 14. The minimum pressure shows relatively large deviations within the nasal cavity: not only in the first points (56% in 1R, 4.0 Pa, and 67% in 1L, 4.0 Pa), but also further into the nasal cavity with differences around 30% at points 3 and 4 (2.6-3.4 Pa), and differences between 19 and 26% at points 5 and 6 (1.9–3.2 Pa). The largest absolute deviations are found at points 14 and 16, respectively 5.8 (18%) and 7.0 Pa (13%).

Corresponding mean and maximum pressures during exhalation are shown in Fig. 5a and b. The maximum pressures are in very good agreement (deviations of typically less than 1 Pa or 1–6%) within both nasal cavities and in the larynx, but larger discrepancies are observed in the nasopharynx and oropharynx (2–3 Pa or 17–36%). The largest absolute deviations are 3.2 Pa (18%) at point 12 and 3.0 Pa (12%) at point 17. The mean pressures show similar results, and the largest differences are 1.8 Pa at point 1R (91%) and 1.5 Pa at points 12 (14%) and 17 (9%).

3.2 Flow characteristics during inhalation and exhalation

Figure 6 shows the instantaneous velocity magnitudes across several cross-sectional planes in the nasal cavity during peak inhalation. Due to the narrowing of the nostril, the flow accelerates distal to the trachea depicted by the minor vortices in planes 9 and 10. The flow attained an average maximum velocity of 1.97 times the inlet velocity in the left nasal valve and an average maximum velocity of 2.76 times the inlet velocity in the right valve. The maximum velocity magnitude during peak inhalation decreases slowly from the nasal valve towards the nasopharynx, but stays within the order of magnitude.

These findings are highlighted in Fig. 7 that depicts fluctuations in the flow field in the lower part of the ethmoid sinus and in the oflactory region. Past the conchae the flow accelerates towards the pharynx. These fluctuations are caused by the narrowing of the nostril as was mentioned above. At the pharynx, a flow jet is observed, which results in vortices and flow separation close to the walls. The peak Reynolds number at the pharynx reached around 4356 during inhalation. Post the nasopharynx area, the geometry diverges around the oropharynx before entering the larynx. At the smallest cross-section in the larynx, the area is 78 mm^2, more than two times smaller than the cross-sectional area of trachea. The complexity of the geometry results in a continuous formation of jets and vortices that merge and annihilate. The maximum velocity observed from Fig. 7 is about 11.2 m/s.

Similar to inhalation, the expiratory velocity magnitudes across the same cross-sectional planes are shown in Fig. 8.

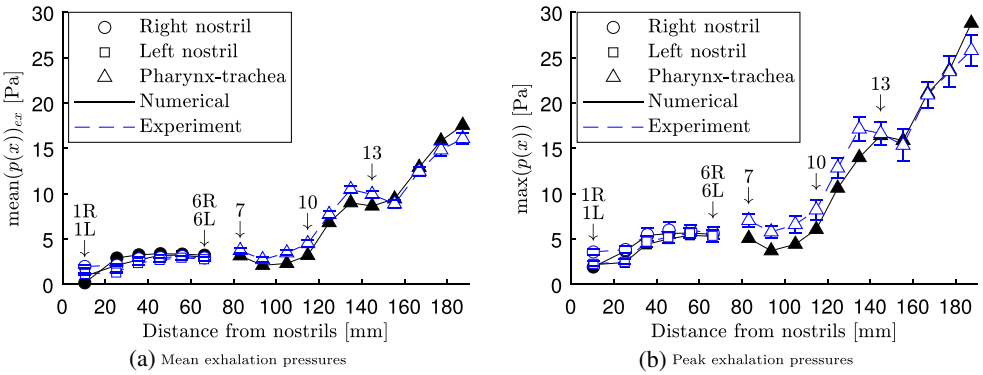

(a) Mean exhalation pressures (b) Peak exhalation pressures

Fig. 5 Exhalation: comparison of pressure obtained from simulations (filled symbols, black) and experiments (open symbols, blue) at the locations depicted in Fig. 1. Error bars for experimental data indicate ±standard deviation of the corresponding values from the individual full breathing cycles

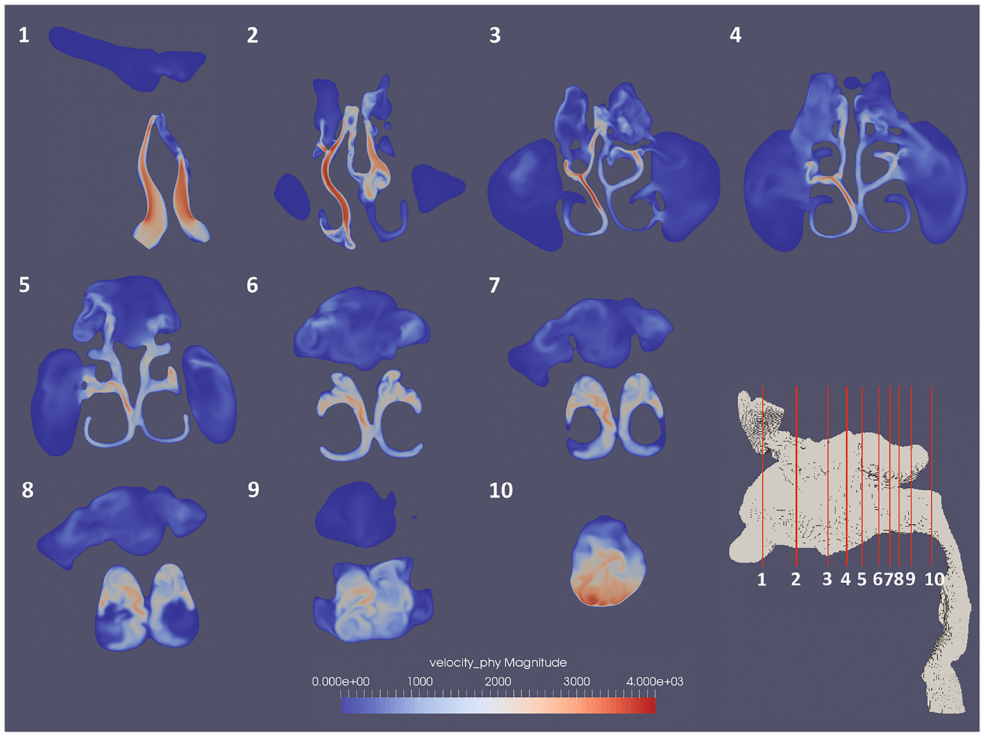

Fig. 6 Velocity magnitude (mm/s) across several cross-sectional planes (posterior view) during peak inhalation (22.13 L/min)

Again minor flow fluctuations are seen in planes 10 and 9. The jet impingement is however more localized now compared to inhalation, resulting in much higher velocities close to the walls.

Very similar trends can be seen in Fig. 9. As the flow progresses through the larynx into the oropharynx, the geometry diverges before converging again in the nasopharynx, creating a second jet there. The jets are however more localized compared to those during inhalation (Fig. 7). Whereas during inhalation the oropharyngeal jet extents through the remainder of the pharynx and ends only close to the larynx, the laryngeal jet during exhalation breaks down in vortices after a shorter length. Also the nasopharyngeal jet during exhalation is relatively local due to the impingement on the roof of the nasopharynx. Recirculating flow is observed near the pharyngeal jet at the anterior site and near the laryngeal jet at posterior site due to flow separation. The pharyngeal jet mostly points upwards, causing the flow to enter the nasal cavities most dominant near the superior nasal concha. As the flow progresses towards the nostrils, the stream distributes more evenly over the cross section.

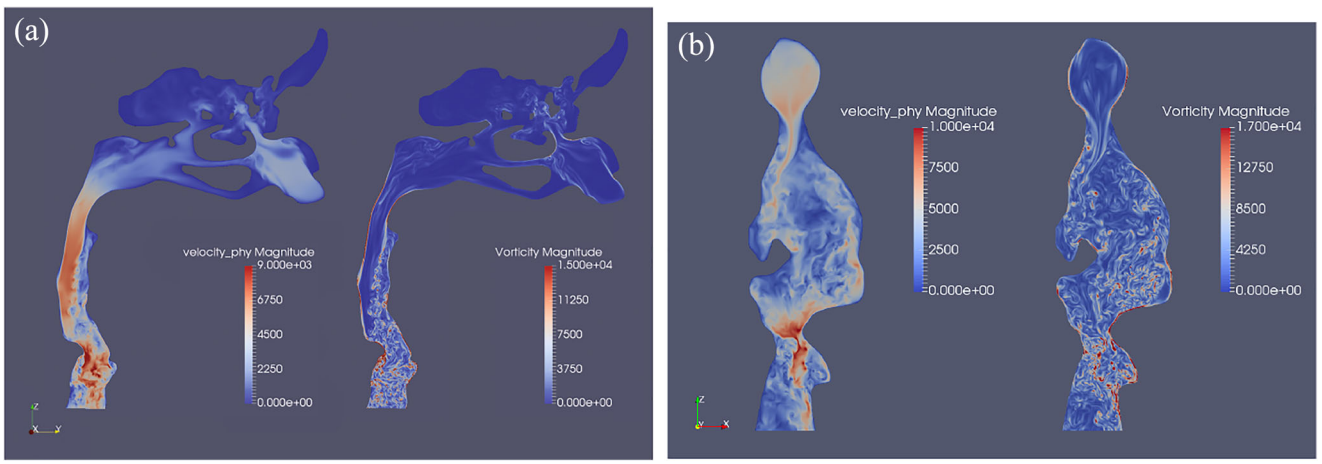

Fig. 7 Velocity (mm/s) and vorticity (1/s) magnitudes across two bisecting perpendicular planes in the geometry. The flow profiles are plotting during peak inhalation

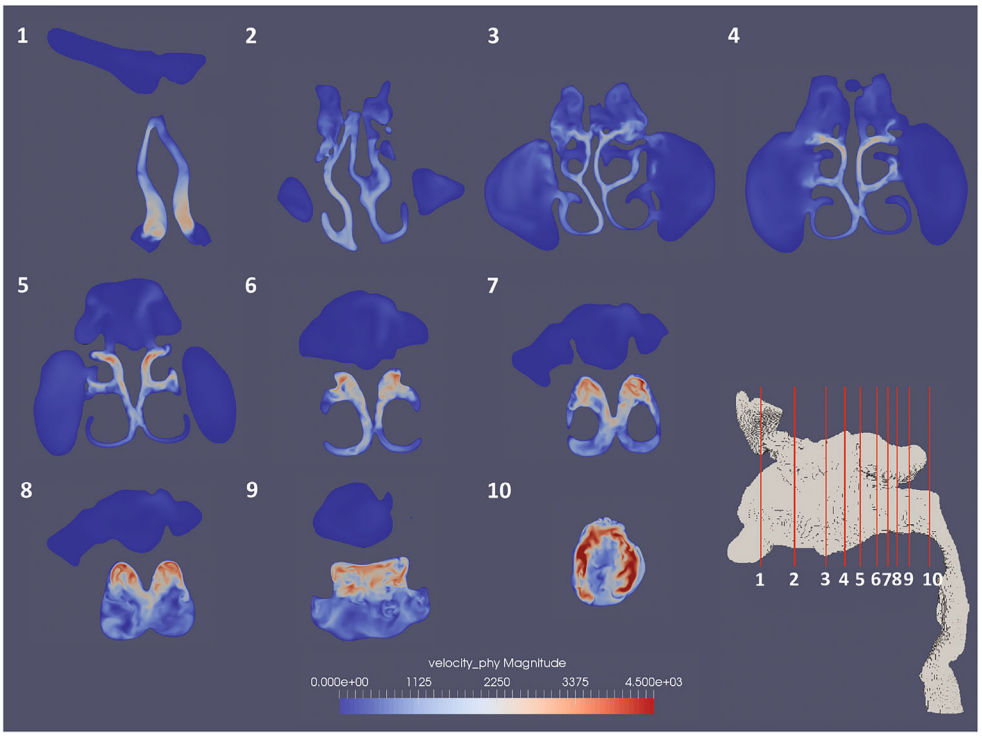

Fig. 8 Velocity magnitude (mm/s) across several cross-sectional planes (posterior view) during peak exhalation (16.0 L/min)

4 Discussion

This work presents the velocity profiles in the human upper airways obtained from LBM/LES simulations. The pressures along the airway were compared with experimental data.

4.1 Comparison of simulations and experiments

The pressures from simulations and experiments are in general in good agreement, except for the first point in both nostrils (1L and 1R). Since the first points are located very close to the nostrils, this difference is presumably caused by local flow differences due to the specified boundary conditions. The pressure is set to atmospheric pressure at the nostrils during the simulations, but this may be different from the actual situation. During inhalation, the flow around the nostril may best be described as sink flow [18], and the pressure at the sink is lower than atmospheric pressure [47]. Hence, the nostril pressure is expected to be below atmospheric pressure during inhalation, but the exact value is unknown and probably dependent on the nostril geometry and the breathing profile [47]. During exhalation, a diverging (conical) jet is expected [18]. For these types of

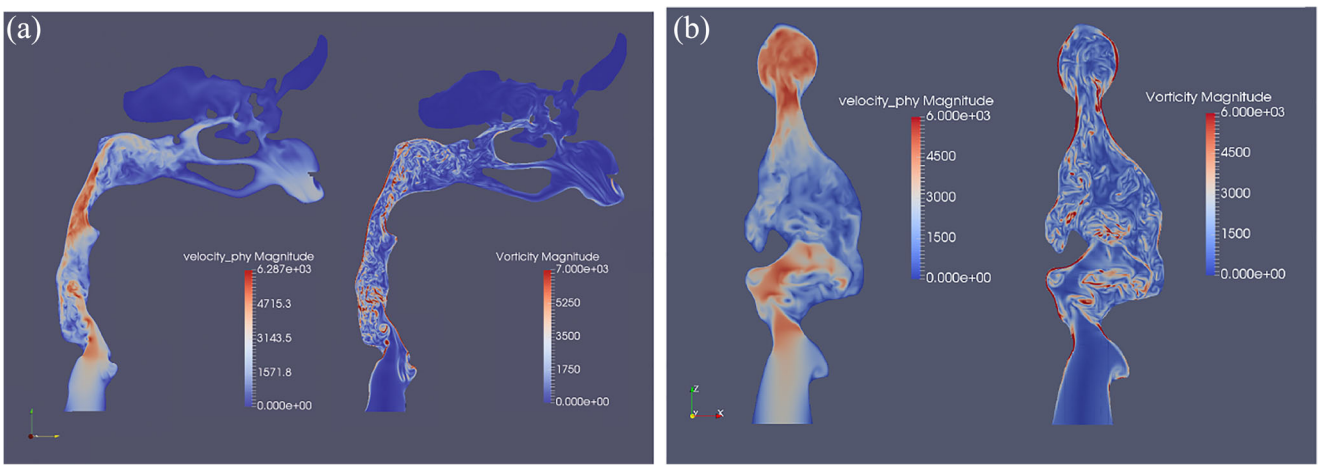

Fig. 9 Velocity (mm/s) and vorticity (L/s) magnitudes across two bisecting perpendicular planes in the geometry. The flow profiles are plotting during peak exhalation

jets, the pressure at a nozzle exit is higher than atmospheric pressure [24], and hence it is expected that the nostril pressure is slightly above atmospheric pressure during exhalation. The boundary condition mainly influences the pressure drop between the nostrils and the nasal valve [44], such that the numerical and experimental pressures are in good agreement from point 2 onwards.

During inhalation, the mean pressure is in very good agreement within the nasal cavity and the nasopharynx (with errors typically around 7%), whereas more deviations of approximately 10–15% are observed from oropharynx to trachea. From the velocity and vorticity magnitudes in Fig. 7, local transition of flow to turbulence is evident from the appearance of vortices. During peak inhalation, larger differences are observed within the nasal cavity. These differences can be explained by the low pressure values in the nasal cavity, making it more sensitive to measurement errors. In the mean pressure, the measurement errors are averaged out. The pressures at points 14 and 16 during peak inhalation show the largest differences. It is seen in Fig. 7 that these locations show the highest vorticity magnitudes. The corresponding rapid variations in pressure make the comparison of the pressure at a specific point and at a specific time (i.e., peak inhalation) very sensitive to change. By taking the (temporal) mean pressure during inhalation the sensitivity is decreased, but small differences between the specified numerical locations and the experimental pressure taps may still have a large influence. During exhalation, Fig. 9 shows that a turbulent jet is formed in the larynx, such that high vorticity is found in the larynx and oropharynx. A secondary jet is formed in the nasopharynx, again leading to high vorticity. As explained above, a higher vorticity corresponds to rapid variations in pressure, which increases the spatial and temporal sensitivity of the pressure. This may explain the larger differences between the numerical and experimental pressures at peak exhalation between points 7 and 13. The mean exhalation pressures, however, are in very good agreement. Point 17 also shows a relatively large deviation, especially at peak exhalation. During the simulations, fully developed flow is specified at the trachea. During the experiments, the trachea is connected to the breathing simulator by a tube with relatively small diameter. Point 17 is located close to the narrower connection and may therefore not be well representative of the physical situation. Nonetheless, the good agreement between the simulations and the experiments show that LBM combined with LES is an adequate tool for simulating flows in the airway. Combining LBM and LES has the potential to reveal the flow dynamics of respiratory support therapies like nasal high-flow therapy, although the associated higher Reynolds numbers will increase computational effort. Therefore, advanced collision operators might be explored in future.

4.2 Clinical flow characteristics

In this section, some important clinical features of the flow are discussed. It is observed that, in both inhalation and exhalation, the flow is accelerated in the nasal valve. This is expected from the area constriction and was also observed in earlier studies [7, 40, 41, 46, 48]. Behind the nasal valve, the velocities during inhalation are highest in the middle meatus, indicating that this is the main flow region. In the upper part of the nasal cavity, near the olfactory region, increased velocity and recirculation is observed. Although increased velocity and recirculation are presumably beneficial for the sense of smell [27], it seems to be highly anatomy-dependent [7, 46, 48, 49, 52].

During exhalation, the flow is more evenly spread in the frontal part of the nasal cavity, but mainly flowing through the top region of the nasal cavity and the superior meatus at the back part. This is caused by the nasopharyngeal jet that impinges on the roof of the nasal cavity, such that flow enters the nasal cavity at the top. Clinically, the different flow patterns during inhalation and exhalation can be an explanation for the earlier perceived differences in airway resistance during inhalation and exhalation [48].

In the nasopharynx, a turbulent jet is observed during exhalation, marked by high vorticity magnitudes. During inhalation, flow is also accelerating in the nasopharynx (due to contraction of the airway), but the jet itself remains mostly laminar. However, vortices are formed in the anterior side of the oropharynx at the boundary of the jet. At this point, the flow shows more turbulent fluctuations in the larynx and in the trachea. During exhalation, flow was still laminar in the trachea (which was prescribed as boundary condition), but departs from a laminar regime in the larynx. The flow pattern in the pharynx is of particular interest for obstructive sleep apnoea, since anatomically the pharynx is the part of the upper airway most vulnerable to collapse due to the lack of bony support on the anterior and lateral walls [35]. The turbulent vortices on the anterior side of the oropharynx may lead to an increased inward force on the airway walls and cause airway collapse.

The resistance of the airway, which is equal to the pressure drop divided by the flow rate, is an important factor for the effort of breathing [1, 39]. By looking at the pressure drop, the airway regions with the highest resistance can be identified. During inhalation, the nasopharynx (between points 8 and 10) and the larynx (between points 14 and 15) contribute most significantly to the pressure drop. Unsurprisingly, these are the same regions where flow was found to accelerate. The contraction of the airway leads to high velocities and high resistance. During exhalation, the largest pressure drops are observed in the larynx (between points 16 and 14) and in the oropharynx (between points 12 and 10). In both inhalation and exhalation, the nasal cavity accounts

for less than 20% of the pressure drop over the model. This strongly contradicts some earlier studies, where the nasal cavity accounts for 70–90% of the pressure drop in the upper airway [12, 37, 48]. However, the pressure drop in the nasopharynx was shown to exceed the pressure drop over the nasal cavity in [46], which does agree to the present study. Although more research is needed on the partitioning of airway resistance, the results in the present study clinically imply that constrictions in the larynx and pharynx may have the most significant effect on the resistance in the upper airway, but this is presumably depending on the individual airway anatomy.

4.3 Limitations

This study has some limitations. First, it is noted that the geometry used in this study has a nasal septum perforation from plane 4 towards the nasopharynx (see Fig. 6). The connection between both nasal cavities may have influenced flow dynamics, and different flow structures may therefore be observed in other geometries. However, comparison of flow dynamics in individual nasal cavities is always difficult due to the large heterogeneity in the anatomical structure [5].

Secondly, the velocity boundary conditions used in this study were simplified: during inhalation, a uniform flow was assumed at the nostril inlet. The ratio of flows through both nostrils was estimated from low Reynolds number simulations to have equal nostril pressure, resulting in a maximum error of 5% in the higher Reynolds number simulations. In order to improve this, some part of the atmosphere around the nose may be included in the computational domain, such that the two nostrils are merged to one inlet. In this way, flow can distribute naturally over both nostrils. This will also improve the calculation of the nostril pressure, improving the results close to the nostrils.

Thirdly, the effects of heating and humidification of air were neglected in this study (both in simulations and in experiments).

Finally, only one geometry was studied, which may limit the clinical relevance. However, the comparison of the simulations to experiments in the same geometry does show the potential of combined LBM/LES in determining airflow dynamics, which opens the route to further computational studies with multiple geometries.

5 Conclusion

Numerical simulations of a full breathing cycle in a human upper airway from nose to trachea have been demonstrated using a combination of LBM and LES. Pressure data were compared to experimental data in a 3D print of the same geometry. The simulations and experiments show some deviations in regions of turbulent flow at peak inhalation and exhalation, but are on average in good agreement. The simplified boundary condition of atmospheric nostril pressure influences the flow close to the nostrils. In general, it is concluded that LBM combined with LES is an adequate tool for simulating flows in the human nasal airway.

The simulations demonstrate pharyngeal and laryngeal jets with high velocity magnitudes during exhalation and inhalation. Also the pressure drop, indicating resistance, is most significant at these locations. The pressure drop over the nasal cavity was relatively low: less than 20% of the pressure drop over the model. Furthermore, recirculation in the region of the olfactory cleft is observed.

In future work, multiple geometries should be simulated to gain further understanding of the respiratory dynamics. An important potential application of combined LBM/LES is to reveal the flow dynamics of respiratory therapies like nasal high-flow therapy, although more advanced collision operators might be explored to overcome the increased computational effort due to higher Reynolds numbers.

Appendix: Mesh convergence study

To ensure that the computed solution did not depend on the spatial and temporal resolutions, a mesh convergence study was performed in the case of nasal airflow. Previous findings on suitable mesh sizes for oscillatory [26] and transitional flows [25] were used to get an initial estimate. The convergence study was conducted because nasal airflows were being simulated for the first time using the LBM solver *Musubi*, and LES turbulence model was being employed. In the mesh convergence study, the breathing velocity profile was scaled to $\frac{1}{8}$th of its value to save computing resources.

The spatial and temporal resolutions chosen are listed in Table 1.

The L_1 norm is calculated for the velocity magnitude, where the L_1 is defined as the mean of the sum of the absolute differences between the velocity magnitudes on the

Table 1 Spatial (δx) and temporal (δt) resolutions as well as the lattice sites for various mesh densities studied in the mesh convergence study

	δx (mm)	δt (μs)	nCells (M)
h_1	0.20	10.8	12.2
h_2	0.175	8.3	18.4
h_3	0.15	6.1	29.5
h_4	0.125	4.2	51.3
h_5	0.10	2.7	101
h_6	0.09	2.2	139
h_7	0.075	1.5	241

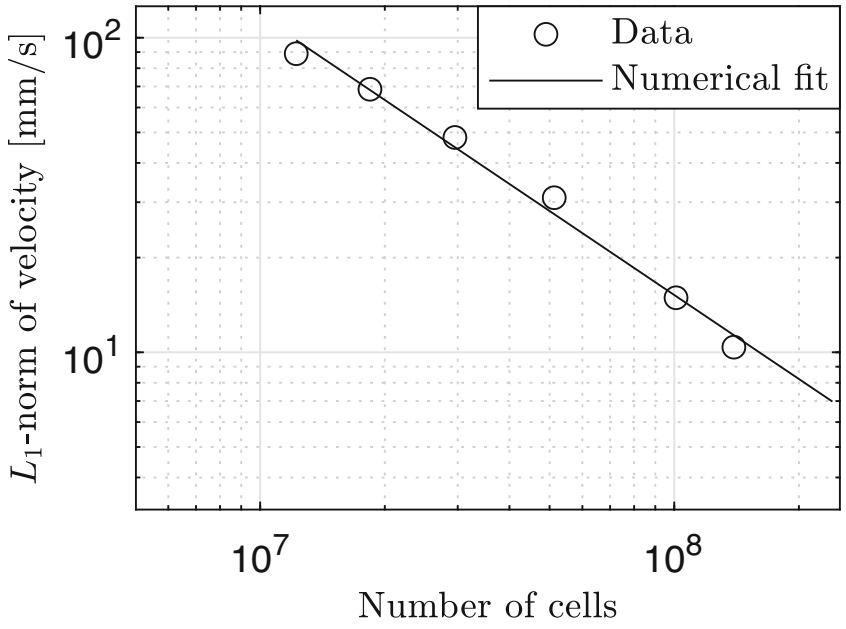

Fig. 10 L_1 norm (mm/s) of the velocity magnitude

grids and the velocity magnitude on the finest grid ($\delta x = 0.075$ mm) on each time step:

$$L_1 = \frac{1}{N}\sum_{t=1}^{N}\left(|U_t - U_{t,0.075}|\right) \tag{5}$$

The results are shown in Fig. 10. It can be seen that the velocity norm decreases linearly for most of the resolutions. Due to the transient nature of the flow, there is a slight fluctuation at resolution h_4, which settles down at finer resolutions. Thus, it is inferred that this resolution is sufficient for the simulation of nasal airflow reported in this article. Based on these findings and the scaling of the breathing profile, the resolution of 0.048 mm was employed that resulted in 925 M cells. Further details about lattice parameters and their scaling can be referred in [25].

Funding Compute resources on the Dutch national supercomputer Cartesius were provided by SURFSara through NWO grant 2019/ENW/00768083.

Declarations

Ethics approval Not applicable: the authors did not collect data from any human participant or animal.

Conflict of interest The authors declare no competing interests.

References

1. Adams C, Geoghegan PH, Spence CJ, Jermy MC (2018) Modelling nasal high flow therapy effects on upper airway resistance and resistive work of breathing. Respir Physiol Neurobiol 254:23–29
2. Berger M, Pillei M, Giotakis A, Mehrle A, Recheis W, Kral F, Kraxner M, Riechelmann H, Freysinger W (2021a) Pre-surgery planning tool for estimation of resection volume to improve nasal breathing based on lattice Boltzmann fluid flow simulations. Int J Comput Assist Radiol Surg 16(4):567–578
3. Berger M, Pillei M, Mehrle A, Recheis W, Kral F, Kraxner M, Bardosi Z, Freysinger W (2021b) Nasal cavity airflow: comparing laser doppler anemometry and computational fluid dynamic simulations. Respir Physiol Neurobiol 283:103533
4. Bouzidi M, Firdaouss M, Lallemand P (2001) Momentum transfer of a Boltzmann-lattice fluid with boundaries. Phys Fluids 13:3452
5. Brüning J, Hildebrandt T, Heppt W, Schmidt N, Lamecker H, Szengel A, Amiridze N, Ramm H, Bindernagel M, Zachow S, Goubergrits L (2020) Characterization of the airflow within an average geometry of the healthy human Nasal Cavity. Scient Rep 10(1):3755
6. Chen W, Wang L, Chen L, Ge H, Cui X (2022) Numerical study of the impact of glottis properties on the airflow field in the human trachea using v-LES. Respir Physiol Neurobiol 295:103784
7. Chung S-K, Kim SK (2008) Digital particle image velocimetry studies of nasal airflow. Respir Physiol Neurobiol 163(1):111–120
8. Cui X, Ge H, Wu W, Feng Y, Wang J (2021) LES study of the respiratory airflow field in a whole-lung airway model considering steady respiration. J Brazilian Soc Mech Sci Eng 43(3):141
9. Cui X, Wu W, Ge H (2020) Investigation of airflow field in the upper airway under unsteady respiration pattern using large eddy simulation method. Respir Physiol Neurobiol 279:103468
10. Doorly DJ, Taylor DJ, Schroter RC (2008) Mechanics of airflow in the human nasal airways. Respir Physiol Neurobiol 163(1):100–110
11. embodi3D.com (2016) Easily create 3D printable muscle and skin STL files from medical CT scans. https://www.embodi3d.com/blogs/entry/353-easily-create-3d-printable-muscle-and-skin-stl-files-from-medical-ct-scans/
12. Ferris BG, Mead J, Opie LH (1964) Partitioning of respiratory flow resistance in man. J Appl Physiol 19(4):653–658
13. Finck M, Hänel D., Wlokas I. (2007) Simulation of nasal flow by lattice Boltzmann methods. Comput Biol Med 37(6):739–749
14. Fomin VM, Vetlutsky VN, Ganimedov VL, Muchnaya MI, Shepelenko VN, Melnikov MN, Savina AA (2010) Air flow in the human nasal cavity. J Appl Mech Techn Phys 51(2):233–240

15. Geller S, Krafczyk M, Tölke J., Turek S, Hron J. (2006) Benchmark computations based on lattice-Boltzmann, finite element and finite volume methods for laminar flows. Computers & Fluids 35(8):888–897
16. Goodarzi-Ardakani V, Taeibi-Rahni M, Salimi MR, Ahmadi G (2016) Computational simulation of temperature and velocity distribution in human upper respiratory airway during inhalation of hot air. Respir Physiol Neurobiol 223:49–58
17. Harlacher DF, Hasert M, Klimach H, Zimny S, Roller S (2012) Tree based voxelization of stl Data. High performance computing on vector systems, 81-92
18. Haselton FR, Sperandio PG (1988) Convective exchange between the nose and the atmosphere. J Appl Physiol 64(6):2575–2581
19. Hasert M (2014) Multi-scale Lattice Boltzmann simulations on distributed octrees. PhD thesis, Aachen, Techn Hochsch., Diss., 2013
20. Hasert M, Masilamani K, Zimny S, Klimach H, Qi J, Bernsdorf J, Roller S (2014) Complex fluid simulations with the parallel tree-based lattice Boltzmann solver Musubi. J Comput Sci 5(5):784–794
21. Hebbink RHJ, Duiverman ML, Wijkstra PJ, Hagmeijer R (2022) Upper airway pressure distribution during nasal high-flow therapy. Med Eng Phys 104:103805
22. Hebbink RHJ, Hagmeijer R (2021) Tidal spirometric curves obtained from a nasal cannula. Med Eng & Phys 97:1–9
23. Hörschler I, Schröder W, Meinke M (2010) On the assumption of steadiness of nasal cavity flow. J Biomech 43(6):1081–1085
24. Hrycak P, Jachna S, Lee DT (1974) A study of characteristics of developing, incompressible, axi-symmetric jets. Letters in Heat and Mass Transfer 1(1):63–71
25. Jain K (2020a) Efficacy of the FDA nozzle benchmark and the lattice Boltzmann method for the analysis of biomedical flows in transitional regime. Medical & Biological Engineering & Computing 58:1817–1830. PMID:32507933
26. Jain K (2020b) Transition to turbulence in an oscillatory flow through stenosis. Biomech Model Mechanobiol 19:113–131. PMID:31359287
27. Keyhani K, Scherer PW, Mozell MM (1997) A numerical model of nasal odorant transport for the analysis of human olfaction. J Theor Biol 186(3):279–301
28. Klimach H, Jain K, Roller S (2014) End-to-end parallel simulations with apes, vol 25, pp 703-711
29. Krafczyk M, Tölke J, Luo L-S (2003) Large-eddy simulations with a multiple-relaxation-time lbe model. Int J Mod Phys B 17(01n02):33–39
30. Lee J-H, Na Y, Kim S-K, Chung S-K (2010) Unsteady flow characteristics through a human nasal airway. Respir Phys Neurobiol 172(3):136–146
31. Leonard A (1975) Energy cascade in large-eddy simulations of turbulent fluid flows. 18, 237–248
32. Lintermann A, Meinke M, Schröder W (2013) Fluid mechanics based classification of the respiratory efficiency of several nasal cavities. Comput Biol Med 43(11):1833–1852
33. Mihaescu M, Murugappan S, Kalra M, Khosla S, Gutmark E (2008) Large eddy simulation and Reynolds-averaged Navier-Stokes modeling of flow in a realistic pharyngeal airway model:, an investigation of obstructive sleep apnea. J Biomech 41(10):2279–2288
34. Phuong NL, Yamashita M, Yoo S.-J. (2016) Andamp; Ito, K. Prediction of convective heat transfer coefficient of human upper and lower airway surfaces in steady and unsteady breathing conditions. Building and Environment 100:172–185
35. Pierce R, Worsnop C (1999) Upper airway function and dysfunction in respiration. Clin Exp Pharmacol Physiol 26(1):1–10
36. Riazuddin VN, Zubair M, Abdullah MZ, Ismail R, Shuaib IL, Hamid SA, Ahmad KA (2011) Numerical study of inspiratoryand expiratory flow in a human nasal cavity. J Med Biol Eng 31(3):201–206
37. Rohrer F (1915) Der strömungswiderstand in den menschlichen Atemwegen und der Einfluss der unregelmässigen Verzweigung des Bronchialsystems auf den Atmungsverlauf in verschiedenen Lungenbezirken. Pflüger's Archiv für die gesamte Physiologie des Menschen und der Tiere 162(5):225–299
38. Roller S, Bernsdorf J, Klimach H, Hasert M, Harlacher D, Cakircali M, Zimny S, Masilamani K, Didinger L, Zudrop J (2012) An adaptable simulation framework based on a linearized octree. High performance computing on vector systems, 2011, 93-105
39. Scott JB, Kaur R (2020) Monitoring breathing frequency, pattern, and effort. Respir Care 65(6):793–806
40. Spence CJT, Buchmann NA, Jermy MC (2012) Unsteady flow in the nasal cavity with high flow therapy measured by stereoscopic PIV. Exp Fluids 52(3):569–579
41. Spence CJT, Buchmann NA, Jermy MC, Moore SM (2011) Stereoscopic PIV measurements of flow in the nasal cavity with high flow therapy. Exp Fluids 50(4):1005–1017
42. Succi S, Benzi R, Higuera F (1991) The lattice Boltzmann equation: a new tool for computational fluid-dynamics. Physica D 47(1):219–230
43. Tabe R, Rafee R, Valipour MS, Ahmadi G (2021) Investigation of airflow at different activity conditions in a realistic model of human upper respiratory tract. Comput Methods Biomech Biomed Engin 24(2):173–187
44. Taylor DJ, Doorly DJ, Schroter RC (2010) Inflow boundary profile prescription for numerical simulation of nasal airflow. Journal of The Royal Society Interface 7(44):515–527
45. Van Hove SC, Storey J, Adams C, Dey K, Geoghegan PH, Kabaliuk N, Oldfield SD, Spence CJT, Jermy MC, Suresh V, Cater JE (2016) An experimental and numerical investigation of co2 distribution in the upper airways during nasal high flow therapy. Ann Biomed Eng 44(10):3007–3019
46. Van Strien J, Shrestha K, Gabriel S, Lappas P, Fletcher DF, Singh N, Inthavong K (2021) Pressure distribution and flow dynamics in a nasal airway using a scale resolving simulation. Phys Fluids 33(1):011907
47. Voropayev SI (2015) Pressure distribution in unsteady sink and source flows. Phys Rev E 91(5):053013
48. Wang Y, Liu Y, Sun X, Yu S, Wang Y, Liu Y, Sun X, Yu S, Gao F (2009) Numerical analysis of respiratory flow patterns within human upper airway. Acta Mech Sin 25(6):737–746
49. Xu C, Khoa ND, Yoo S-J, Zheng X, Shen S, Ito K (2021) Inhalation airflow and ventilation efficiency in subject-specific human upper airways. Respir Physiol Neurobiol 285: 103587
50. Xu X, Wu J, Weng W, Fu M (2020) Investigation of inhalation and exhalation flow pattern in a realistic human upper airway model by PIV experiments and CFD simulations. Biomech Model Mechanobiol 19(5):1679–1695
51. Zhu JH, Lee HP, Lim KM, Lee SJ, San LTL, Wang DY (2013) Inspirational airflow patterns in deviated noses: a numerical study. Comput Methods Biomech Biomed Engin 16(12):1298–1306
52. Zhu JH, Lee HP, Lim KM, Lee SJ, Wang DY (2011) Evaluation and comparison of nasal airway flow patterns among three subjects from Caucasian, Chinese and Indian ethnic groups using computational fluid dynamics simulation. Respir Physiol Neurobiol 175(1):62–69

Rutger Hebbink is a PhD candidate in the Engineering Fluid Dynamics group at the University of Twente, THE NETHERLANDS. He acquired his MSc at the University of Twente.

Bas Wessels obtained his master's degree in Mechanical Engineering at the Engineering Fluid Dynamics group at the University of Twente, The Netherlands.

Dr. Rob Hagmeijer has a PhD degree in aeronautical engineering from Delft University of Technology. He worked at the Dutch National Aerospace Laboratory NLR for more than a decade on hypersonic aerodynamics. Since 2000, he has been an associate professor in fluid dynamics. During recent years, he focused on biomedical fluid mechanics such as respiratory flows and cardiovascular flows.

Dr. Kartik Jain is an assistant professor of Biofluid Dynamics at the University of Twente, THE NETHERLANDS. He acquired his MS and PhD in GERMANY and has previously worked as a postdoc in SWITZERLAND.